Reaction Chemistry & Engineering

ROYAL SOCIETY OF CHEMISTRY

PAPER

View Article Online
View Journal | View Issue

Cite this: *React. Chem. Eng.*, 2024, **9**, 1845

Received 18th December 2023,
Accepted 24th March 2024

DOI: 10.1039/d3re00689a

rsc.li/reaction-engineering

Enhancing mass transport to accelerate photoreactions and enable scale-up†

Florian Gaulhofer,[a] Markus Metzger,[a] Alexander Peschl[b] and Dirk Ziegenbalg *[a]

The importance of mixing in photoreactors along the direction of light propagation for competitive photochemical reactions is experimentally demonstrated in the MISCOP mini-plant photoreactor. The installation of customized static mixers improved the photonic efficiency of the photochemical ring-opening isomerization of 1,3,3-trimethylindolino-6′-nitrobenzopyrylospirane by a factor of 2.4, which could be related to the improved mass transport. This knowledge enables future scaling of photoreactions in multi-lamp reactors.

1 Introduction

Photochemical conversions are building blocks for the development of sustainable chemical processes, giving access to synthesis routes that are not accessible through thermally induced ground state chemistry. Conducting photoreactions in continuously operated reactors meets many principles of Green Chemistry, such as improved safety, high energy efficiency, and reduced waste.[1–4] Reaction control and overall process performance of photochemical transformations strongly depends on the efficiency and rate of absorption of photons, and the interaction of excited species with other reactants.[5–7] To exploit the synthetic potential of photoreactions, scale-up strategies must be developed that enable a simple transfer from small to large scale. Such strategies must consider the particularities of photoreactors and photoreactions, most importantly: i) the attenuation of light intensity in participating media, ii) technical limitations related to scaling of light sources (*e.g.* electrical connectivity, or reactors), and iii) changing properties of the participating media during the course of the reaction.[8–10]

Gradients in intensity and reaction rate are challenging for reactions during which the absorption properties of the reaction solution change. A prominent example of this kind of photoreaction is the photochemical production of vitamin D3, featuring a complex dynamic equilibrium between four photoisomers, resulting in overlapping absorption spectra and a broad product distribution.[11,12] This competitive reaction network causes self-shadowing in the reaction solution. Without mass transport along the ray trajectory, the reaction progress is limited after photo-stationary equilibrium is reached.[13,14] Thus, mass transport along the direction of light propagation is of utmost importance, not only to cope with the properties of the light-sources in terms of scale-up, but also to address the characteristics of complex reaction networks. Frequently, long residence times are required, associated with laminar flow conditions and slow mass transport, especially perpendicular to the main flow direction.[15,16] Since most photoreactors are irradiated in a cross-current fashion, a strong gradient of the reaction rate potentially leads to lower overall performance and/or product yield.[17–19] The use of static mixers is a meaningful approach to ensure fast mass transport even for laminar flow conditions.[16,20–25] Mixing can also be enhanced by inducing defined vortices, *e.g.* in a Taylor–Couette reactor, which was recently applied to photochemical processes.[26,27] Since mass transport limitations are the major contributor as the reaction rate limiting step, spinning disk technologies are able to intensify photochemical processes by addressing the surface to volume ratio.[28,29]

The advances of microreactors in chemical engineering offered the research field of photochemistry the opportunity to address the challenge of photon transport limitation by using microstructured photoreactors.[30] A wide portfolio of solutions in the field of flow photochemistry at laboratory scale was developed for organic synthesis, material science, and water treatment.[31–40] The scale-up of micro-photoreactors has usually been realized with a numbering up approach to maintain reaction conditions.[41–43] Industrial applications require a systematic scale-up strategy, that starts in the laboratory together with a comprehensive documentation and reporting strategy.[16,44–46] The scale-up of industrial applicable photoreactors must consider two

[a] *Institute of Chemical Engineering, Ulm University, Albert-Einstein-Allee 11, 89081 Ulm, Germany*
[b] *Peschl Ultraviolet GmbH, Weberstraße 19, 55130 Mainz, Germany.*
E-mail: dirk.ziegenbalg@uni-ulm.de

† Electronic supplementary information (ESI) available. See DOI: https://doi.org/10.1039/d3re00689a

geometric challenges: i) the scaling of light sources, *e.g.* internal/external multi-lamp systems, or the increase of lamp length, and ii) the scaling of the reaction volume. The requirement to separate the reaction volume and the light source, and the challenge to control strong gradients of the radiation field lead to the development of complex photoreactor concepts using immersion lamps. Until now, the majority of industrial photochemical reactions are driven by mercury vapour lamps (Hg lamps), but the increasing availability of high power light-emitting diodes (LEDs) in the last decade made their application highly promising for organic photochemistry.[47–50]

The well-established scale-up concept for complex photoreactors using immersion lamps (Hg lamps as well as LEDs) is based on a single unit photoreactor that is scaled up by increasing the reactive volume through one-dimensional scaling of a single unit reactor until the technical limits of the light source are reached. A further scale-up can be achieved by switching to a multi-lamp system.[51] Maintaining similar process experiences for the reacting molecules throughout the scale-up is essential to this concept.[52] For this purpose, a fully characterized single unit photoreactor must be available. The modular, industrial scalable, continuously operated photoreactor (MISCOP) is designed to bridge the gap between laboratory photoreactors (small scale), and industrial photoreactors (large scale). For this reactor, experimental and numerical hydrodynamic studies have shown that the installation of static mixers significantly improves macro-mixing within the mini-plant photoreactor.[16]

In this work, the impact of enhanced mass transport along the direction of light propagation by static mixers in the mini-plant photoreactor was investigated as a basis for a future scale-up of the system. The photochemical ring-opening isomerization of 1,3,3-trimethylindolino-6′-nitrobenzopyrylospirane, driven by an LED immersion lamp, was experimentally studied to benchmark the performance of the MISCOP system. Static mixers were installed in the annular reactor to counteract performance limitations caused by the self-shadowing effect of the photoisomerization. The experimental results in the mini-plant photoreactor were complemented with numerical computations of the radiation field of the mini-plant photoreactor to evaluate the photonic efficiency for a variation of reactor configurations and operating points.

2 Experimental methods

2.1 Chemicals

1,3,3-Trimethylindolino-6′-nitrobenzopyrylospirane (CAS: 1498-88-0, M = 322.36 g mol^{-1}) was purchased from TCI Development Co., Ltd. Technical grade ethanol (96 vol%, TechniSolv™) from VWR International Ltd, and analytical grade ethanol (99.5 vol%, EMPLURA™, Supelco™) from Merck were used as solvents. The spiropyrane powder was dissolved in ethanol with a Palssonic PTIC-10-ES ultrasonic bath (ALLPAX GmbH, Germany).

2.2 Analytical methods

Online UV/vis spectroscopy was conducted with a balanced deuterium halogen lamp AvaLight-DH-S-BAL, two optical fibres FC-UV600-2-BX and a AvaSpec-ULS2048 spectrometer (all Avantes BV, Netherlands). Self-designed mounts for the optical fibres were used as measuring cells and fitted to the process tube.[53] Video footage was recorded with a Sony ZV-1 camera (Sony Europe B.V, UK), and 420 nm and 645 nm long pass filters (SCHOTT GG420 and SCHOTT RG645, Edmund Optics, Ltd).

2.3 Cuvette reactor

A cuvette setup (Fig. 1) allowed for simultaneous UV/vis absorbance measurements and irradiation of the reaction solution in a cuvette to determine the spectral Napierian absorption coefficient. A 1 cm quartz glass cuvette was placed in a 3D printed mount with two collimating lenses on opposite sites. Optical fibres (FC-UV600-2-BX, Avantes BV, Netherlands) were used to connect the lenses to the spectrometer and the light source. An LED was placed above the cuvette with a scaffold and used to irradiate the cuvette from above. The forward reaction (Fig. 6) was initiated by a 365 nm UV LED (SMD-LED NVSU233A, Nichia Co., Japan) mounted on a cuboid heat sink. The backward reaction was initiated with a 530 nm LED (LST1-01F06-GRN1-00, New Energy, USA) mounted on a star-shaped printed circuit board (Opulent Americas, USA) and a star-shaped heat sink was utilized. The cuvette was equipped with a magnetic stirring bar and the setup was placed on a magnetic stirrer Hei-Mix L (Heidolph Instruments GmbH), operated at a stirring speed of 400 rpm.

2.4 Modular photoreactor

The recently presented mini-plant photoreactor MISCOP (Modular Industrial, Scalable Continuously Operated Photoreactor) with axial inlet configuration (V2-AX) was utilized to study static mixing elements.[16] The axial inlet is not disturbing the inlet section of the photoreactor, and thus enables an accurate evaluation of static mixing elements compared to a tangential inlet. The modularity of this reactor enabled flexible changes of the setup, and allowed convenient experimental investigation of static mixers (Fig. 2a). The photoreactor consisted of a head and bottom module enclosing a cylindrical glass reactor jacket of

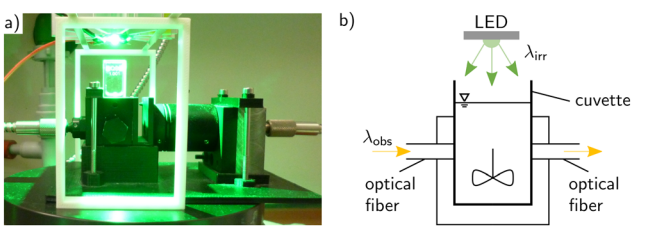

Fig. 1 a) Picture of the cuvette reactor during irradiation with a 530 nm LED. b) Schematic view of the cuvette setup.

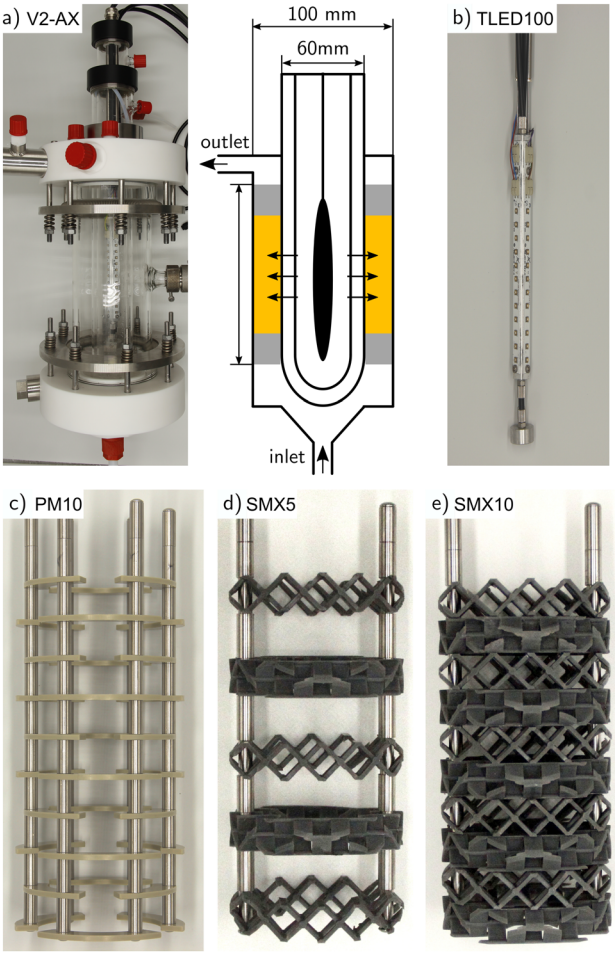

Fig. 2 a) Picture and scheme of the V2-AX photoreactor. The characteristic annular geometry (grey) and the irradiation zone (yellow) are highlighted. b) Picture of the LED immersion lamp TLED100 and the investigated static mixer: c) PM10, d) SMX5, e) SMX10.

250 mm length and an outer diameter of 100 mm. The outer diameter of the cladding tube system was 60 mm, constituting a total reactor volume of 1.63 L. The photoreactor was equipped with an LED immersion lamp novaLIGHT TLED100 (365 nm, Peschl Ultraviolet GmbH, Germany) depicted in Fig. 2b. The emitted radiometric power P_{LED} of the TLED100 was dimmable in a range of 5% to 100%. The maximal emitted radiometric power P_{max} of 43.2 W corresponded to a maximum emitted photon flux q^{em}_{pmax} of 132 µmol s^{-1}. Two types of static mixers were investigated: a plate mixer with 10 plates (PM10) and a SMX™-type mixer with 5 and 10 elements (SMX5 and SMX10, respectively; see Fig. 2c–e).

The MISCOP reactor was manufactured by Peschl Ultraviolet GmbH. The head and bottom module were made of polytetrafluoroethylene (PTFE), the reactor jacket was fabricated out of borosilicate glass, and the cladding tubes were made out of quartz glass. GL connectors for analytic and process ports were installed (Bohlender GmbH, Germany). The plate mixers were made from polypropylene (PP). The SMX internals were 3D printed out of synthetic resin with a Low Force Stereolithography (LFS™) 3D-printer Form3L (Formlabs GmbH, Germany). Baffle plates were 3D printed out of polylactic acid (PLA) with a Fused-Deposition Modelling (FDM) 3D-printer Pro2 Plus (Raise 3D, USA). The annular static mixers were fixed in position by a stainless steel (A4) mounting system in both reactor setups, and the standard height of packings was set to 200 mm.

Experimental setup. The equipment was installed into a infraCabinet and a photonCabinet of the Modular Photochemical Development System (MPDS) (Peschl Ultraviolet GmbH, Germany). An overview of the setup is given in Fig. 3. A polytetrafluoroethylene (PTFE) tube with inner diameter of 12 mm and outer diameter of 14 mm (Bohlender GmbH, Germany) connected a MD-100FX rotary pump (Iwaki Co., Ltd, Germany), a 5 L glass tank, and the photoreactor (V2-AX). A vane flow meter (KOBOLD Messring GmbH, Germany) was used to measure the flow rate. The operating points were set to $\dot{V}$ = 4 and 8 L min^{-1}, corresponding to Reynolds numbers of 350 and 700 for ethanol. The bypass for the UV/vis measurements was realized with a perfluoroalkoxy alkane (PFA) tube with an inner diameter of 4.37 mm and the UV/vis measurement cell was attached to the tube. The LED immersion lamp was cooled by a ThermoControl unit (dark blue). The outlet temperature of the photoreactor was measured by a thermocouple type K connected to a Thermocouple Bricklet 2.0 and a Master brick 2.1 (Tinkerforge GmbH, Germany).

Experimental procedure. Prior to the experiments, the system was purged with nitrogen. Subsequently, the reaction solution containing 1,3,3-trimethylindolino-6′-nitrobenzopyrylospirane **1** in technical grade ethanol ($c_{1,0}$ = 0.37 mol L^{-1}) was cycled through the setup with a flow rate $\dot{V}$ at ambient temperature (T_{am} = 21 °C). After t_0 = 20 s from measurement start, the LED immersion lamp was

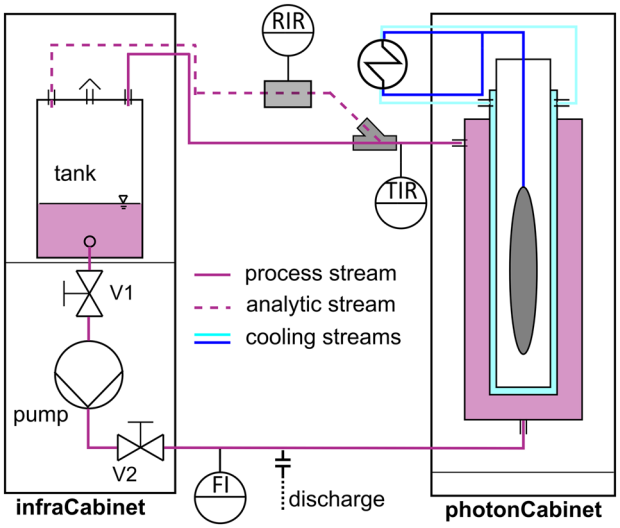

Fig. 3 Flowchart of the experimental setup of the axial MISCOP. Measuring points in the flowchart are noted according to ISO3511 for indicated flow rates (FI), indicated and recorded temperatures (TIR), and indicated and recorded radiation (RIR).

switched on and the reaction proceeded until a quasi steady-state of a single pass of the reactor was reached. The outlet concentration was recorded by online UV/vis measurements of absorbance A at 540 nm in the bypass (Fig. 3).

3 Numerical methods

3.1 Radiative transport

Fig. 4 shows the propagation of radiant energy (photons) represented by bundles of rays with a given energy schematically. The rays are described by the incident spectral radiance (spectral specific intensity), which is the fundamental property for characterizing radiation fields. dS is an arbitrarily oriented small area with the spatial coordinate $\vec{x}$, P a point in this area, and $\vec{n}$ the normal to the area at point P. At a given time, rays will pass through this area element in all directions.

A balance of all incoming and outgoing fluxes through this balance element requires constitutive relations to describe phenomena like absorption, emission, and in/out scattering. A specific direction $\vec{\Omega}$ coincides with the axis of an elementary cone of solid angle dΩ and $\vec{\Omega}$ is characterized by the unit direction vector $\vec{\Omega}$ with the angle θ to the normal $\vec{n}$.

All elementary solid angles, corresponding to rays parallel to the direction $\vec{\Omega}$ passing through dS, define a truncated semi-infinite cone dω, having a cross-sectional area perpendicular to the point P d$S\cos\theta$. dP_λ is the total amount of radiant energy passing through the area dS inside the cone in the time dt and with an energy of the wavelength range between λ and λ + dλ. The incident spectral radiance is defined as:[5,54]

$$L_{\lambda,\vec{\Omega}}(t,\vec{x}) = \lim_{\mathrm{d}S,\mathrm{d}\Omega,\mathrm{d}t,\mathrm{d}\lambda\to 0} \frac{\mathrm{d}P_\lambda}{\mathrm{d}S\cos\theta\mathrm{d}\Omega\mathrm{d}t\mathrm{d}\lambda} \tag{1}$$

There is no fundamental difference between the incident spectral radiance L_λ and the incident spectral photon flux density $L_{\mathrm{p},\lambda}$, as the unit conversion is a constant:

$$L_{\mathrm{p},\lambda} = L_\lambda \cdot \frac{\lambda}{N_\mathrm{A}\cdot h\cdot c}, \tag{2}$$

with the wavelength of the photon λ, the Avogadro constant N_A, the Planck's constant h and the speed of light c. The radiative transport equation for a homogeneous medium for absorption without scattering and emission effects is expressed as:[5,55–58]

$$\frac{\mathrm{d}L_{\lambda,\vec{\Omega}}(\vec{x},t)}{\mathrm{d}s} = -\alpha_\lambda L_{\lambda,\vec{\Omega}}(\vec{x},t), \tag{3}$$

where $\frac{\mathrm{d}L_{\lambda,\vec{\Omega}}(\vec{x},t)}{\mathrm{d}s}$ is the directional derivative along the direction s at a point $\vec{x}$ in the reaction space of the incident radiance. The linear Napierian absorption coefficient α_λ is expressed as:

$$\alpha_\lambda = \sum_{i=1}^{I} \kappa_{\lambda,i} c_i, \tag{4}$$

with the Napierian absorption coefficient $\kappa_{\lambda,i}$ of species i at a wavelength λ and concentration c_i of species i. Integrating the radiative transport equation (RTE) over all directions $\vec{\Omega}$ of the incident radiance $L_{\lambda,\vec{\Omega}}(\vec{x},\ t)$, and assuming monochromatic light λ_1 results in the spherical fluence rate $E_\mathrm{o}(\vec{x},\ t)$:

$$E_\mathrm{o}(\vec{x},t) = \int_{\lambda_1}^{\lambda_1}\int_{\vec{\Omega}} L_{\lambda,\vec{\Omega}}(\vec{x})\mathrm{d}\vec{\Omega}\mathrm{d}\lambda_1. \tag{5}$$

No time dependency is considered due to the speed of light, and summation over all cells c in the region k of the absorbed local radiance $L^\mathrm{a}(\vec{x}) = \alpha E_\mathrm{o}(\vec{x})$ gives the total absorbed radiant flux q_k^a in region k:

$$q_k^\mathrm{a} = \sum_{c=1}^{C} L_{\mathrm{c},k}^\mathrm{a}(\vec{x})\cdot V_\mathrm{c}, \tag{6}$$

with V_c as the cell volume of the mesh.

The most widespread numerical methods used to solve the RTE are the discrete ordinate method (DOM) and the Monte Carlo method.[59–62] The RTE was solved with the open source software OpenFOAM v7.[63] The solver multiRegionRadiationFOAM incorporates two main features: 1) choice of an emission model of the light source and 2) solving the RTE from the surface of a light source through multiple regions (multi-region) with varying absorption properties and optical boundaries in a 3D mesh, utilizing the discrete ordinate method (DOM).[57,58] The meshes were generated with snappyHexMesh, and the number of cells per mesh are given in Table 2. The visualisation of the mesh quality is shown in the ESI† (Fig. S2). The preconditioned bi-conjugate gradient (PBiCGStab) numerical solver together with the preconditioner DILU was used with absolute tolerances of 1×10^{-6}. Directional discretization of ordinates of 15 for both angles in an octant was applied, resulting in 1800 ordinates (15 × 15 × 8) in each region. Parallel computing was realized with 48 processors on the JUSTUS2 cluster on a large, fast I/O (FAT) node with 1536 GB memory. The total memory requirement of the solver for a 64 bit architecture is extremely high due to the number of ordinates calculated. Thus, the mesh refinement was adjusted to use the full capacity of the FAT nodes.

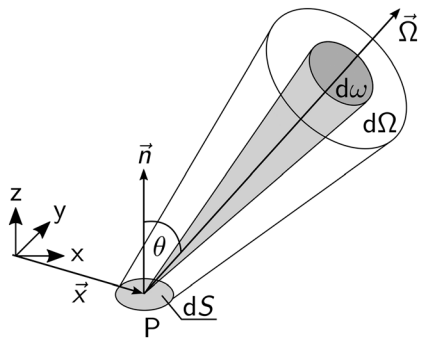

Fig. 4 Schematic representation of a bundle of rays (photons) characterizing the radiation field. Adopted from Cassano *et al.*[5]

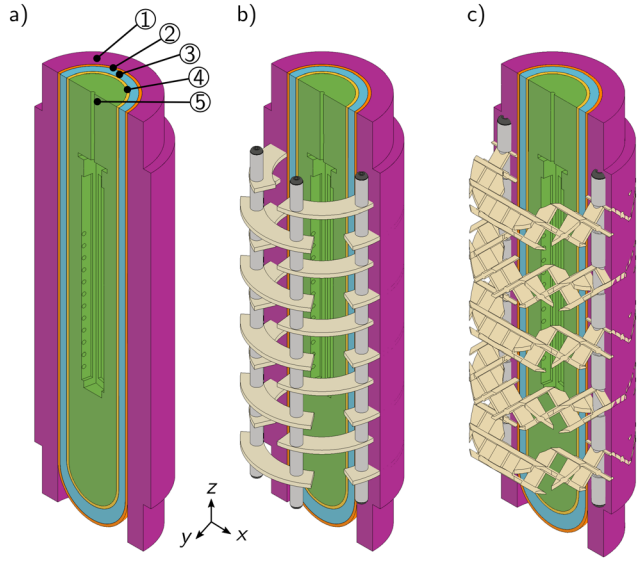

Fig. 5 CAD representation of the regions of the photoreactor with an LED immersion lamp, and static mixers: a) empty photoreactor (EMPTY), photoreactor equipped with b) a plate mixer with 10 units (PM10), and c) a SMX mixer with 5 units (SMX5). The multi-region setup is colour-coded and contains the following single phase regions: 1) reactor volume, 2) outer cladding tube, 3) cooling fluid, 4) inner cladding tube, and 5) nitrogen gas.

3.2 Multi-region case

Fig. 5 a depicts the geometry of the mini-plant photoreactor, divided into five defined regions:

1. internal reactor volume filled with reaction solution (purple),
2. outer cladding tube made of quartz glass (orange),
3. cooling jacket filled with water (blue),
4. inner cladding tube made of quartz glass (yellow),
5. gas phase around the lamp filled with nitrogen (green).

Fig. 5b and c illustrate the mixer regions inside the reactor, which were simulated as an additional region 6.

The irradiation was assumed to be monochromatic, and an isotropic emission was used as emission model. The surface of the LED lenses were chosen as a source term for radiative transport. The initial radiance L^0_{LED} at the surface of a single LED was defined as a function of electrical operating conditions and initialized as:

$$L^0_{\mathrm{LED}} = \frac{P_{\max}}{S_{\mathrm{LED}}} = \eta_{\mathrm{el}} \cdot \frac{U \cdot I}{S_{\mathrm{LED}}} = 63\,660\ \mathrm{W\ m^{-2}}, \tag{7}$$

with the electricity-to-radiation efficiency η_{el}, voltage U, electrical current I, and the surface area of one LED lens S_{LED}.

Absorption of light by water, nitrogen and quartz glass was neglected. Thus, optical properties of non-absorbing media were chosen ($\alpha = 1 \times 10^{-2}\ \mathrm{m^{-1}}$). Static mixers were set to possess full absorption by assigning a large linear Napierian absorption coefficient ($\alpha = 1 \times 10^{4}\ \mathrm{m^{-1}}$). The absorption in the reaction solution was defined by eqn (4) with the experimentally used initial concentrations $c_{1,0}$ and Napierian absorption coefficients κ. The boundary condition of each region was set to be transmissive, except for the mount of the UV LED immersion lamp, which was set to be reflective, since the materials were aluminium and stainless steel.

3.3 Photochemical performance indicators

The photonic efficiency ξ, defined by IUPAC, is the ratio of the rate of the photoreaction measured for a specified time interval and the rate of incident photons $q^0_{\mathrm{p},\lambda}$ within a defined wavelength interval inside the reactor:[56]

$$\xi = \frac{\mathrm{d}n_i/\mathrm{d}t}{\int_{\lambda_1}^{\lambda_1} q^0_{\mathrm{p},\lambda}\mathrm{d}\lambda}. \tag{8}$$

LEDs emit photons with a narrow bandwidth,[64] which is often assumed monochromatic: $\int_{\lambda_1}^{\lambda_2} q^0_{\mathrm{p},\lambda}\mathrm{d}\lambda = q^0_{\mathrm{p}}$. The incident photon flux q^0_{p} is often unknown and is approximated by experimental and numerical methods (actinometry, radiometry, CFD, ray tracing) as the absorbed photon flux $q^{\mathrm{a}}_{\mathrm{p}}$ of the reaction solution.

In general, the emitted photon flux $q^{\mathrm{em}}_{\mathrm{p}}$ represents a more accessible metric. The efficiency of guiding photons from the light source to the reactor includes the optical properties of the entire reactor setup and only leaves the electricity-to-photons efficiency, and thus the required electrical power, as an open parameter. The external efficiency can be calculated from experimental data with:

$$\zeta_{\mathrm{ext}} = \frac{\mathrm{d}n_{\mathrm{i}}/\mathrm{d}t}{q^{\mathrm{em}}_{\mathrm{p}}} = \frac{\frac{\Delta c_2}{\Delta t}\cdot(V_{\mathrm{R}} - V_{\mathrm{l}})}{q^{\mathrm{em}}_{\mathrm{p}}}. \tag{9}$$

The performance of photoreactions is governed by the absorbed photon flux $q^{\mathrm{a}}_{\mathrm{p}}$ in the reaction domain. The total reactor is a multi structure system, which contains the reaction domain as well as potential additional installations, such as static mixers. If additional installations are present, the amount of photons available to the reaction solution is reduced by absorption of those installations. Thus, it is important to determine the fraction of light which is available for the photoreaction. To quantify this fraction, the transmittance of internals T_{int} into a region k that is equipped with mixers is defined as the ratio of the radiant density that is absorbed under full absorption q^{a}_k (eqn (6)) in a region k to the emitted radiant flux q^{em} by the light source:

$$T_{\mathrm{int},k} = \frac{q^{\mathrm{a}}_k}{q^{\mathrm{em}}}. \tag{10}$$

In the absence of internals and in the case of total absorption of the reaction solution, the transmittance of internals into the reaction solution equals one. If internals, such as static mixers, are installed, the fraction of photons absorbed by the static mixers must be subtracted.

The photonic efficiency ξ is used to evaluate the efficiency of photoreactors:

$$\xi = \frac{\mathrm{d}n_i/\mathrm{d}t}{q^{\mathrm{a}}_{\mathrm{p}}}. \tag{11}$$

The absorbed photon flux $q^{\mathrm{a}}_{\mathrm{p}} = T_{\mathrm{int}} \cdot q^{\mathrm{em}}_{\mathrm{p}}$ is correlated to the emitted photon flux of a light source through the

transmittance of internals. Based on experimental results, ξ is calculated as:

$$\xi = \frac{\frac{\Delta c_2}{\Delta t}\cdot(V_R - V_l)}{q_p^a} = \frac{\frac{\Delta c_2}{\Delta t}\cdot(V_R - V_l)}{T_{int}\cdot q^{em}} = \frac{\xi_{ext}}{T_{int}}, \quad (12)$$

with the volume of the reactor V_R filled with reaction solution $V_R - V_l$, where V_l is the volume of the mixers (l: = EMPTY, PM10, SMX5, SMX10; Table 2) and the time interval $\Delta t = t_{ss} - t_0$, during which a change of concentration $\Delta c_2 = c(t_{ss}) - c(t_0)$ is recorded (see section 6 for further details).

4 Photophysical and photokinetic properties

4.1 Photochromic reaction system

The isomerization of a spiropyrane was chosen as a benchmark reaction to elucidate the potential impact of a static mixer on mass transport processes in the mini-plant photoreactor (MISCOP). Therefore, preliminary studies on photophysical and photokinetic properties of the spiropyrane dissolved in technical grade ethanol (EtOH (tech)), and analytical grade ethanol (EtOH) were conducted in the cuvette reactor. Fig. 6 illustrates the reversible reaction scheme of the ring-opening photoisomerization of 1,3,3-trimethylindolino-6′-nitrobenzopyrylospirane. The spiropyrane **1** is referenced as closed form, the merocyanine **2** as opened form. Upon UV-irradiation (λ_{irr} = 365 nm) the colourless species **1** isomerizes to the coloured species **2**.[65–69] The spiropyrane is a photochromic compound of type T and P. The reversible back reaction (2 → 1) is induced either by temperature increase of the reaction solution, or by irradiation with green light at a wavelength of about 540 nm. Without UV irradiation, the reaction system equilibrates thermally.

Studies on the thermal ring closure reaction of **2** in EtOH (tech) did not show a significant contribution of the thermal reaction path. A rate constant for the thermal reaction (2 → 1) k_t = 0.0006 min^{-1} and a maximum reaction rate of r_t = 1.6 × 10^{-6} mol m^{-3} s^{-1} was determined for species **2** and c_2 = 0.16 mmol L^{-1} in EtOH (tech). The photochemical reaction rate r_p is estimated from a capillary reactor setup for a low absorbed photon flux of q_p = 7 × 10^{-8} mol s^{-1}, a quantum yield of Φ = 0.17, and volume of the reactor V_R = 0.98 mL as:[67]

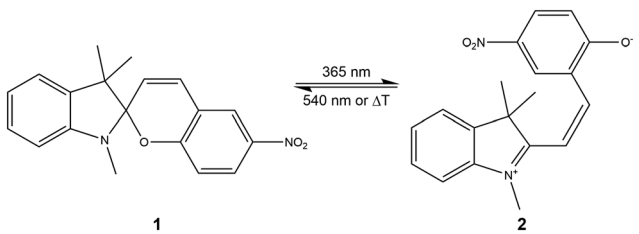

Fig. 6 Reaction scheme of the reversible ring-opening photoisomerization of 1,3,3-trimethylindolino-6′-nitrobenzopyrylospirane **1** to its merocyanine form **2**.

$$r_p = \Phi\cdot\frac{q_p}{V_R} = 0.0121 \text{ mol m}^{-3}\text{ s}^{-1}.$$

The photochemical reaction rate r_p (1 → 2) is about 7500 times faster than the thermal reaction rate r_t (2 → 1). Roxburgh *et al.* reported a rate of thermal decolourization of k_t = 0.02 min^{-1} in methanol, and Aillet *et al.* reported a rate of thermal decolourization of k_t = 0.02 min^{-1} in ethanol.[37,70] Consequently, a minor contribution to the reaction network of the thermal back reaction is assumed, when the experimental time is in the range of minutes.[37,65,68–71] The maximum solubility of spiropyrane **1** was found to be c = 10.8 mmol L^{-1} and c = 6.2 mmol L^{-1} in EtOH and EtOH (tech), respectively.

4.2 Absorption spectra of spiropyrane

The cuvette reactor setup and online UV/vis measurements allowed for measurement of absorption spectra of species **1** and the reaction solution containing both species (mixture). The spectral data of the mixture was obtained under continuous UV-irradiation (λ_{irr} = 365 nm) and stirring until photo-stationary equilibrium was reached. The back reaction towards species **1** was initiated by irradiation with a wavelength of 540 nm. The spectral data was recorded in the concentration range of 0.06 to 0.16 mmol L^{-1}.

Fig. 7 depicts spectral Napierian absorption coefficients $\kappa_{\lambda,i}$ of species **1** and a mixture of species **1** and **2** in EtOH (tech) (—), and EtOH (---). The absorption spectrum of species **1** shows a maximum at 257 nm with a second weaker band at 339 nm. Upon UV-irradiation species **2** forms and a new band evolves at 535 nm. Additionally, a slight bathochromic shift of the band around 339 nm towards 350 nm is noticeable. The band at 540 nm is used to quantify the reaction progress of species **2**. Neither a bathochromic nor a hypsochromic shift of the mixture upon a change of the solvent from EtOH to EtOH (tech) is noticeable, but a clear decrease in the absorption coefficient of the mixture (κ_{mix} (540 nm)) in EtOH (tech) is observed. This is in

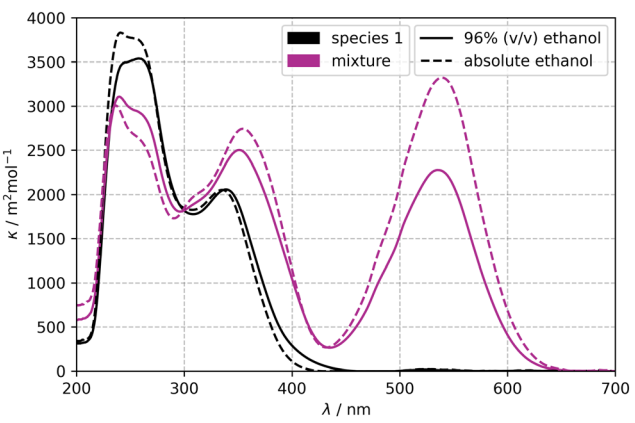

Fig. 7 Spectral Napierian absorption coefficient of **1** and a mixture of species **1** and **2** in EtOH (tech) (—) and EtOH (---).

Table 1 Napierian absorption coefficients κ of spiropyrane (**1**), the mixture of species **1** and **2** (**1** + **2**) and the merocyanine (**2**). The Napierian absorption coefficient of merocyanine **2** was estimated for EtOH (tech)

Species	λ/nm	κ/m^2 mol^{-1}	κ_{est}/m^2 mol^{-1}
1	365	1302[b]	—
	540	—	—
1 + **2**	365	2283[b]	—
	540	2261[b]	—
2	365	4550[a]	3959[c]
	540	7500[a]	5100[c]

[a] Spiropyrane dissolved in ethyl acetate, taken from ref. 68. [b] This work, measured in the cuvette reactor. [c] Values corrected by the solvent dependent correction factor C (eqn (14)).

agreement with a literature description, where more polar solvents shift the visible absorption maximum to shorter wavelengths and lower extinction coefficient.[71]

The isolation of merocyanine **2** is very challenging.[37,66,68,71] To estimate relevant physicochemical parameters related to species **2**, specially designed kinetic experiments must be carried out. Maafi and Brown derived a method that allows the determination of absolute values of the absorption coefficients for species **2** in ethyl acetate (EA).[68] To this point, the absorption spectra of pure species **2** is unknown. Aillet *et al.* conducted investigations on the solvent change from ethyl acetate to EtOH and indicated no prominent changes of the absorption spectra.[37] The solvent change from EtOH to EtOH (tech), which contains water, led to a significant change of the absorption coefficients (Fig. 7). To account for this change, a solvent dependent correction factor C for the Napierian absorption coefficient was introduced for the two characteristic bands at λ = 365 nm and λ = 540 nm:

$$C_1(\lambda = 365\ \text{nm}) = \frac{\kappa_{\text{mix,EtOH(tech)}}}{\kappa_{\text{mix,EtOH}}} = \frac{2283.1\ \text{m}^2\ \text{mol}^{-1}}{2625.1\ \text{m}^2\ \text{mol}^{-1}} = 0.87$$

$$C_2(\lambda = 540\ \text{nm}) = \frac{\kappa_{\text{mix,EtOH(tech)}}}{\kappa_{\text{mix,EtOH}}} = \frac{2260.9\ \text{m}^2\ \text{mol}^{-1}}{3320.5\ \text{m}^2\ \text{mol}^{-1}} = 0.68. \quad (13)$$

The Napierian absorption coefficients estimated for species **2** most likely underestimates the changing absorption characteristics in EtOH (tech), since the reference point of this estimation is the mixture (**1**,**2**) and not pure **2**. Hence, literature values were corrected for the effect of solvent change C:

$$\kappa_{\lambda,\text{EtOH(tech)}} = C_\lambda \cdot \kappa_{\lambda,\text{EA}}. \quad (14)$$

The Napierian absorption coefficients used in this work are listed in Table 1.

4.3 Photodegradation of spiropyrane

Photochromism is a non-destructive process, but side reactions can occur.[66] Usually, the major cause of damage to photochromic substances is oxidation.[72] No detailed information about the degradation mechanism of species **1** is given in literature.[37] The research presented here did not focus on the determination of the photodegradation in EtOH (tech), therefore only preliminary studies were conducted to evaluate the influence on the overall progress of the photoreaction.

Long-term irradiation studies of the spiropyrane dissolved in EtOH (tech) were conducted by operating the mini-plant photoreactor (MISCOP) in recycle mode ($c_{1,0}$ = 0.37 mol L^{-1}, $\dot{V}$ = 4 L min^{-1}). The reaction was driven by an LED immersion lamp (λ_{irr} = 365 nm) at P_{LED} = 100%. The outlet temperature was recorded during the irradiation.

The conversion X_1 is calculated as a function of the measured decadic absorbance A_{obs} at the observation wavelength (λ_{obs} = 540 nm) as follows:

$$X_1 = \frac{A_{obs}}{c_{1,0} \cdot \varepsilon_{est,2}(\lambda_{obs}) \cdot d_i}, \quad (15)$$

with the estimated molar decadic absorption coefficient of species **2** $\varepsilon_{est,2}$, initial concentration $c_{1,0}$, and inner diameter d_i of the bypass capillary.

Fig. 8 shows the temperature T at the outlet of the reactor and the conversion X_1 over the irradiation time t. The temperature increase of 7.4 K during the operation is caused by the exhaust heat of the light source and the pump. A steep increase of X_1 is noticeable, until a maximum conversion of 0.39 was reached at 22 min. The conversion decreases continuously during further irradiation. Two reaction paths contribute to the overall reaction progress during the long-term irradiation: i) the photo-induced reaction that converts species **1** to **2** with rate r_p and ii) the degradation/deactivation/decomposition of species **1** and/or **2**. After t = 22 min, a linear decline of X can be observed. Between 22 min and 60 min, a slightly greater negative gradient of X with a strong positive gradient of T is observed, compared to the time interval 60 to 165 min, where only a slightly lower negative gradient of X with a low gradient of T is observed.

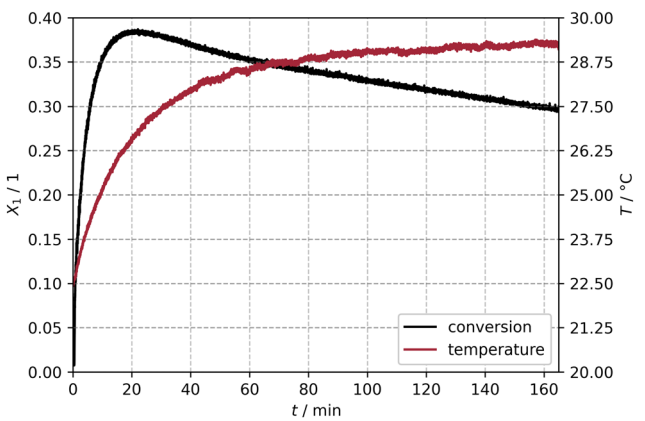

Fig. 8 Conversion X_1 and temperature T of a long-term irradiation (365 nm) of the isomerization of spiropyrane in the mini-plant photoreactor.

The low thermal effect (k_t = 0.0006 min^{-1}) was already discussed for the cuvette reactor, and is assumed negligible for experimental time of 100 s.

After 120 min, the temperature was almost constant, but a continuous decrease of the conversion was observed. Degradation of the spiropyrane, either the open or closed form, during irradiation appears as a possible cause. UV/vis and ^{1}H-NMR measurements gave strong evidence of a degradation process caused by long-term irradiation (see ESI† for further details). Additional substances could be identified, stemming from dissolved mixer material. Due to the short operational time of about 100 s, the influence of side product formation, and dissolution of polymeric compounds from the static mixers on the benchmark experiments is assumed low.

5 Analysis of the radiation field

The determination of the transmittance of internals T_{int} in region k with numerical methods is particularly suited for complex 3D geometries, where radiation models for simple geometries are not suited.[73–76] A simulation of the 3D radiation field of a photoreactor enables quantification of the amount of photons guided into the reaction solution. Alternatively, actinometric or radiometric methods might be utilized to measure the photon flux available to the reaction solution, but in case of the MISCOP these methods are less suited due to the size of the reactor.

The radiation field of the mini-plant photoreactor (MISCOP) was simulated for two different absorption characteristics of the reaction solution containing spiropyrane **1** ($c_{1,0}$ = 0.37 mol m^{-3}) for monochromatic irradiation (λ = 365 nm) with an LED UV immersion lamp. As the reaction proceeds and merocyanine **2** isomerizes, the absorption property of the reaction solution changes (Fig. 7). Therefore, two limiting cases for the time-dependent reaction progress $\left(1 \overset{h\nu}{\rightarrow} 2\right)$ were considered:

- a solution containing only species **1** ($\alpha_1 = \kappa_1 c_{1,0}$),
- and a mixture of **1** and **2** ($\alpha_2 = (\kappa_1 + \kappa_{mix}) c_{1,0}$).

Fig. 9a and b present 1D graphs of the 3D radiation field. The evolution of the local radiance L at z = 125 mm (middle of the light source) along the x-direction on a logarithmic scale is shown for the two limiting cases (Fig. 9a, α_1, α_2). The local radiance L decreases for x = 10 to 30 mm (region 5 to 2) due to the isotropic emission model, but not through absorbing effects, since the corresponding media are chosen to be non-absorbing. A steep decline of L is observed, when photons travel into the reaction solution (region 1). The larger absorptivity α leads to a stronger decline in the local radiance L.

Fig. 9b depicts the local radiance L in region 1 along the z-direction (axial) on a logarithmic scale. The comparison of two different transversal positions at x = 30 mm and x = 32 mm elucidates a strong decline of L_{max} to 1/4 or 1/20 for α_1 and α_2, respectively. In addition, the irradiated volume

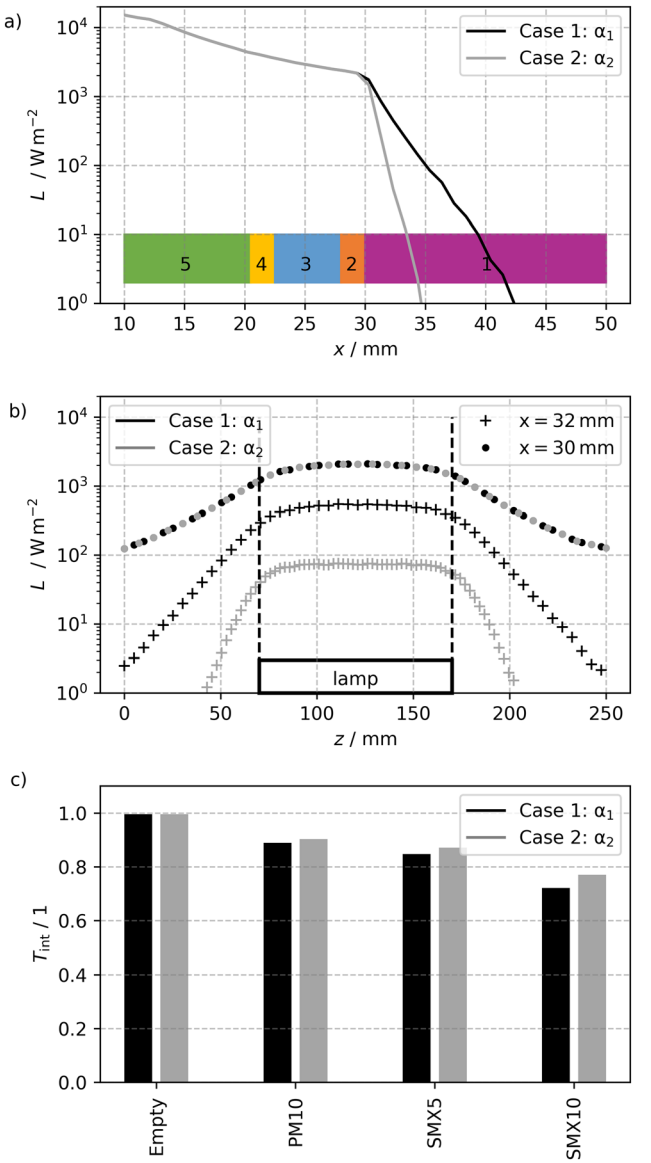

Fig. 9 a) Local radiance L along the x-direction with colour-coded regions of the mini-plant photoreactor. b) Local radiance L along the z-axis at two different positions inside the reactor volume (region 1). The irradiation zone corresponds to the region between $z \approx$ 70 mm and $z \approx$ 170 mm along which LEDs are installed (Fig. S1†). c) Transmittance of internals in region 1 for different geometries T_{int} (EMPTY, PM10, SMX5, SMX10) and photophysical properties (α).

is reasonably mapping the length of the light source (z = 70 to 170 mm), with a steep decline of L at each end of the light source.

Fig. 9c displays the transmittance of internals $T_{int,1}$ in the reaction domain (region 1) for four configurations (EMPTY, PM10, SMX5, SMX10) and the two defined absorption cases (see also Table 2). The photon flux incident on the reaction solution is governed not only by the properties of the reaction solution, but also the installations (mixers) within the reactor geometry. Since the static mixers are not optical transparent, light is absorbed when hitting the solid material. The extent of absorption caused depends on the geometry and number

Table 2 Configuration and results of the radiation field simulations. The cells used in the OpenFOAM simulation, the transmittance of internals T_{int} for α_1 and α_2, and the mixer volume V_l are listed

Mixer ID	EMPTY	PM10	SMX5	SMX10
Cells 1×10^6	4.2	13.6	15.1	21.7
$T_{int}(\alpha_1)/1$	1	0.89	0.85	0.72
$T_{int}(\alpha_2)/1$	1	0.90	0.87	0.77
V_l/L	—	0.1423	0.1170	0.1964

of the mixers. The plate mixer (PM10) possesses a larger absorbable photon flux in region 1 ($T_{int,1}(\alpha_1) \approx 0.89$) compared to the SMX mixers, which have a greater projection area and thus reduce the absorbable photon flux (SMX5: $T_{int,1}(\alpha_1) \approx 0.85$, SMX10: $T_{int,1}(\alpha_1) \approx 0.72$). A large absorptivity α led to shorter penetration depths in the solution. Thus, less light reaches the mixing elements and therefore cannot be blocked. Consequently, higher values of $T_{int,1}(\alpha_2)$ for all static mixers were calculated.

6 Effect of mass transport on self-shadowing photoreactions

6.1 Visualisation of the reaction zone

A recent experimental and numerical hydrodynamic study revealed a significant enhancement of radial and axial mass transport in the mini-plant photoreactor, when static mixers are utilized.[16] Due to the characteristic competitive absorption, the spiropyrane isomerization is an excellent method to study mass transfer limitations in photoreactors, that eventually allows the characterization of different internals in the modular mini-plant photoreactor.

Fig. 10a displays video footage recorded during the irradiation of the reaction solution with the UV LED immersion lamp (365 nm) for the PM10, SMX5, and SMX10 mixers. The video footage reveals significant blockage of light for SMX structures compared to PM mixers. Increasing the number of units also increases the blockage of photons (Fig. 10a). The yellow colour around the light source stems from fluorescence of the merocyanine form **2** that occurs upon irradiation with UV radiation (Fig. 10c). The white regions (Fig. 10a) correspond to high UV radiation, which overlaps with the florescence of species **2**. By installation of cut-off filters (420 nm and 645 nm) in front of the camera, UV light and parts of the visible light could be filtered out. The pictures recorded with the filters only show the fluorescence of species **2** and thus indicate the concentration field of the merocyanine form in the reactor (Fig. 10b). Detailed inspection of the pictures reveals an inhomogeneous concentration field, indicated by changing colour intensity, especially noticeable in the empty reactor. The flow conditions in the different setups are visible in the videos provided as ESI† (filenames indicate reactor setup and use of filter). The fluid motion, indicated by colour changes, is clearly visible for video footages with and without filter.

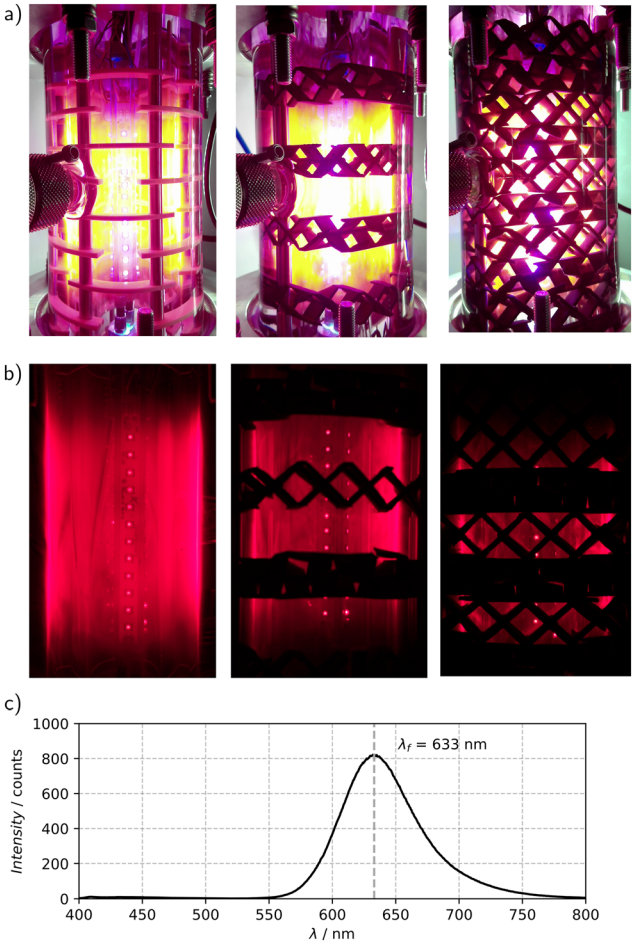

Fig. 10 a) Video footage at the end of the experiment for three reactor configurations (PM10, SMX5, SMX10). The yellow colour corresponds to fluorescence of species **2**. b) Video footages with 645 nm long pass filters, solely showing the fluorescence of **2** for three reactor configurations (EMPTY, SMX5, SMX10). c) Fluorescence spectrum of substance **2** (λ_{exc} = 365 nm).

6.2 Effect of static mixer on mass transport

Fig. 11 displays the conversion X_1 (eqn (15)) of the benchmark reaction for different configurations of the MISCOP ($\dot{V}$ = 4 L min^{-1}, P_{LED} = 100%). The LED immersion lamp is turned on at t_0 = 20 s. For all configurations, the first change of conversion is detected after $t \approx 5$ s, followed by a characteristic increase of the conversion for each mixer configuration. The empty reactor yields the lowest conversion, compared to configurations with static mixers. The experimental run of the empty reactor was carried out at an initial conversion $X_{1,0} > 0$, since the reaction solution was still in thermal equilibrium. The concentration fluctuations of species **2** in the empty reactor is due to the hydrodynamic instabilities. Vortex formation in the inlet section was observed, and these vortexes moved subsequently into the annular reaction zone of the reactor.[16]

Adding the PM10 (green) to the reaction zone leads to greater conversion, as well as to a reduction of fluctuations.

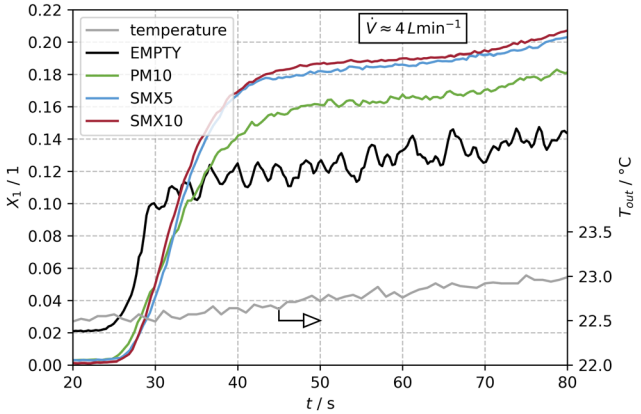

Fig. 11 Conversion X_1 and temperature T_{out} during the benchmark reaction for different mini-plant photoreactor (MISCOP) configurations: EMPTY, PM10, SMX5 and SMX10.

The SMX structures (blue, red) show the highest conversion, whereby an increase in the number of SMX structures has only a marginal influence. After $t \approx 1.5\tau$, an increase in conversion for all configurations is observed due to operating the reactor in recycle mode and the change of the inlet concentration associated with this. The small temperature increase of 0.5 °C within 80 s, measured at the outlet of the reactor, allows assuming isothermal operation and thus a negligible impact of the thermal back reaction for the evaluation.

To further quantify the impact of different hydrodynamic conditions, additional reactive experiments were conducted for a flow rate $\dot{V}$ of 8 L min^{-1} and different photon fluxes, realized by changing the power of the LED immersion lamp P_{LED}.

Fig. 12a shows the conversion at $t = t_{ss}$ for varying power of the LED immersion lamp P_{LED}. At $t_{ss} = 1.5\tau_l$, a steady-state of a single pass of the reactor is assumed, with the hydrodynamic residence time τ_l of the corresponding reactor configuration. The individual hydrodynamic residence time $\tau_l = \frac{(V_R - V_l)}{\dot{V}}$ can be calculated from the reactor volume V_R and the mixer volume V_l, (l: = EMPTY, PM10, SMX5, SMX10; Table 2). The installation of the SMX structures resulted in the highest conversion of X_1 = 0.186, whereas the EMPTY configuration only yields X_1 = 0.114. With decreasing photon flux and increasing flow rate, the conversion reduces.

All configurations were also evaluated by means of the external photonic efficiency ξ_{ext} (eqn (9)). The most demanding reaction conditions in terms of absolute reaction rate gradients are present when operating the lamp with P_{max}. Consequently, the strongest impact of mass transport limitations are expected for these conditions. The following observations regarding the external photonic efficiency (Fig. 12b) at P_{LED} = 100% are imminent: i) ξ_{ext} increases with the installation of static mixers, ii) a higher flow rate results in greater ξ_{ext}. Lowering the power of the LED results in greater ξ_{ext} with a maximum at P_{LED} = 25%. At lamp power $P_{LED} < 100\%$, the SMX5 consistently shows higher ξ_{ext} than

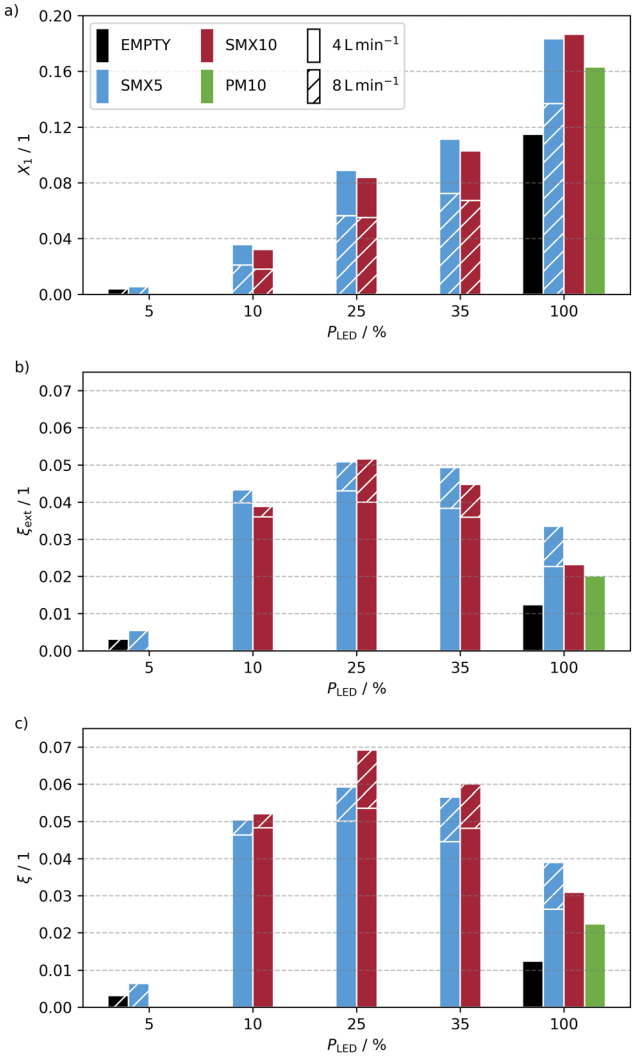

Fig. 12 Conversion X_1 (a), external photonic efficiency ξ_{ext} (b), and photonic efficiency ξ (c) determined for the photoisomerization at two flow rates and varying power of the LED immersion lamp P_{LED}. The PM10 mixer was experimentally evaluated only for P_{max}.

the SMX10. The superior performance of SMX5 is reasoned by the negative impact of the larger blockage of light by the SMX10 structures. The performance order of static mixers is: SMX5 ≥ SMX10 > PM10. Consequently, the PM10 was excluded from further investigations due to poor performance compared to the SMX structures.

To differentiate the effect of mass transport from the effect of shadowing on the reactor performance, the computational results of the radiation field were considered (Fig. 9c). For that, the photonic efficiency ξ was calculated. For the self-shadowing reaction under investigation, the photonic efficiency relates the time for mass transport along the ray trajectory with the reaction time. If sufficient reactant is provided for the reaction by a fast mass transport, the photonic efficiency will be increased.

Fig. 12c shows the photonic efficiencies ξ of all experimentally investigated reactor configurations. For

P_{LED} = 100% and $\dot{V}$ = 4 L min^{-1}, the utilization of the SMX10 mixer compared to no static mixer (EMPTY) led to an improvement of the photonic efficiency by a factor of 2.4 from 1.2% to 3.1%. Increasing the flow rate $\dot{V}$ and/or reducing the power of the LED immersion lamp P_{LED} led to an increase of the photonic efficiency ξ. The highest photonic efficiency of about 7% was determined for P_{LED} = 25%, $\dot{V}$ = 8 L min^{-1}, and the SMX10 mixer. Experiments at P_{LED} = 5% are likely falsified by technical limitations in accurately controlling the light output. These technical limitations do not exist at powers of 10%, but efficiencies already tend to appear lower compared to P_{LED} = 25%. The decrease in photonic efficiency for very small photonic fluxes can possibly be explained by the lower mass transfer due to the lower concentration gradient. This leads to a change in the ratio of reaction and mass transport time. A strongly absorbing layer of species **2** forms directly on the wall, which is only transported off very slowly and therefore absorbs the incident photons.

Analysis of the photonic efficiency revealed a change of the order of the static mixers with respect to the reactor performance, and in all cases the SMX10 mixer showed a superior performance. Installation of additional mixing elements causes a more frequent radial redirection of the fluid, which further enhances the overall mass transport along the direction of light propagation. Higher flow rates led to higher flow velocities and thus enhanced radial mass transport.

The photonic efficiency is well suited to be correlated to mass transport effects since the photonic efficiency excludes side effects such as shadowing by the mixing structures. Generally, the trends observed for the photonic efficiency are in line with the hydrodynamic evaluation of the different mixers.[16] The fastest radial mass transport was found for the SMX mixing structures. Considering the annular characteristic of the reactor and the laminar flow conditions, transversal mass transport is required to minimize back-mixing and to overcome the parabolic velocity profile, which ultimately results in a narrowing of the residence time distribution. Thus, large Bodenstein numbers Bo correlate with a fast radial mass transport, as shown previously with the help of CFD simulations.[16] Therefore, this macroscopic, dimensionless number is suited to indicate the degree of mixing along the ray trajectory. Larger ξ were found for larger Bo.

At a high light intensity of P_{LED} = 100%, increasing reaction rate gradients and shadowing lead to a shrinking reaction zone together with a fast shadowing by species **2**. This increases the demand for mass transport in the reaction zone close to the light source. For the MISCOP studied in this work, an operation with P_{LED} = 25% results in the most efficient use of photons under the chosen operation conditions. At higher intensities, the radial mass transport rates can not compensate the increasing reaction rates and the observable photonic efficiency decreases. Even though that the conversion increases with higher intensities, the increase is lower as to be expected from the increase of the photon flux. In terms of efficiency, this translates to a loss of efficiency by more than a factor of 2. This evaluation demonstrates that analysis of the photonic efficiency is more meaningful for a process development, since the effect of operation conditions on the economics of the operation can be deduced.

The reactive characterization of mass transport processes reveals two relevant influences of the radiation field on the participating media. First, a significant mass transfer demand is induced by the competitive photoreaction, in which the absorption of species **2** inhibits the reaction progress, and second the degree of light absorption of static mixers, which reduces the photons available to the photoreaction due to absorption. Generally, it can be concluded that a synchronization of the timescales of mass transport and reaction is a key criterion for an efficient operation of high-performance photoreactors. In terms of scale-up, this synchronization has to be ensured within the whole reactor and becomes more demanding for high-power light sources. The presented experimental results indicate that the installation of static mixers is a viable strategy to realize the required acceleration of the mass transport. A more detailed analysis of the required radial mass transport and the interaction between the different processes requires comprehensive theoretical studies that allow to analyse reaction and mass transport independently.

7 Conclusion

The performance of photoreactions, in which more than one light absorbing species is present in the reaction solution, is linked to the mass transport capabilities of the used photoreactor. The exponential attenuation of the light intensity causes steep reaction rate gradients. In combination with competitive absorption, the reaction zone is restricted only to a narrow region near the light source, utilizing only a small fraction of the reactor volume. Therefore, the overall conversion as well as the performance of the reactor is limited. Only by ensuring fast mass transport along the direction of light propagation, this limitation can be counteracted.

This experimental and numerical study demonstrates that static mixers are suited to provide the required mass transport acceleration for photoreactions. Especially remarkable when considering the small reaction zone that is characteristic for photoreactions. The results clearly show that macroscopic performance metrics describing radial mass transport, such as the Bodenstein number, can be linked to the performance of the photoreactor. Due to the high mass transport demand in a narrow reaction zone at high light intensities, other metrics are required to correlate mass transport rates along the direction of light propagation with the light intensity. Such correlations are currently in focus of ongoing research.

Understanding the mass transport requirements of photoreactions is key for the development of scale-up strategies. The presented investigation shows that the installation of static mixers is a meaningful approach to

accelerate mass transport and eventually the performance of photoreactors. The overall performance of the investigated MISCOP could further be increased by using optically transparent or translucent static mixers. Furthermore, using static mixers allows for scaling the reactor with the length of the light source, since the required mixing performance can be maintained along the length of the light source.

List of symbols

Abbreviations

CFD	Computational fluid dynamics
DOM	Discrete ordinate method
EA	Ethly acetate
EtOH	Ethanol
LED	Light-emitting diode
MISCOP	Modular, industrial scalable, continuously operated photoreactor
PM	Plate mixer
RTE	Radiative transport equation
SMX	Synonym for Sulzers SMX™-type mixers

Latin letters

S	Area, m^2
A	Absorbance, 1
Bo	Bodenstein number, 1
c	Concentration, mol m^{-3}
C	Solvent dependent correction factor
E	Fluence rate, W m^{-2}
E_p	Photon fluence rate, mol s^{-1} m^{-2}
L_λ	Incident spectral radiance, W sr^{-1} cm^{-3} nm^{-1}
$L_{p,\lambda}$	Incident spectral photon flux density, mol s^{-1} cm^{-3} nm^{-1}
L^a	Absorbed local radiance, W cm^{-3} nm^{-1}
P	Power, W
q	Radiant flux, W
q_p	Photon flux, mol s^{-1}
r	Reaction rate mol m^{-3} s^{-1}
Re	Reynolds number, 1
s	Optical pathway
t	Time, s
T	Material transmittance, 1
V	Volume, m^3
$\dot{V}$	Volumetric flow rate, m^3 s^{-1}
X	Conversion, 1

Greek letters

α	Linear Napierian absorption coefficient, m^{-1}
ε	Decadic absorption coefficient, m^2 mol^{-1}
κ	Napierian absorption coefficient, m^2 mol^{-1}
τ	Hydrodynamic residence time, s
λ	Wavelength, m
Φ	Quantum yield, m
ξ	Photonic efficiency, 1
ξ_{ext}	External photonic efficiency, 1

Superscripts

a	Absorbed
em	Emitted

Subscripts

c	Index of cells
est	Estimated
exc	Excitation
i	Index of species
k	Index of regions
l	Index of static mixers
irr	Irradiation
mix	Mixture
int	Internals
o	Overall
p	Photon based unit
R	Reactor
x	x-Direction
y	y-Direction
z	z-direction
0	Initial

Author contributions

Florian Gaulhofer: conceptualization (supporting), data curation (lead), formal analysis (lead), investigation (equal), methodology (lead), software (lead), validation (lead), visualisation (lead), writing – original draft (lead), review and editing (equal). Markus Metzger: data curation (supporting), formal analysis (supporting), investigation (equal), methodology (supporting), visualisation (supporting), writing – original draft (supporting), review and editing (supporting). Alexander Peschl: conceptualization (equal), funding acquisition (equal), project administration (equal), resources (equal), supervision (supporting), writing – review and editing (supporting). Dirk Ziegenbalg: conceptualization (equal), funding acquisition (equal), methodology (supporting), project administration (equal), resources (equal), supervision (lead), validation (supporting), writing – review and editing (equal).

Conflicts of interest

A. P. is CEO of Peschl Ultraviolet GmbH. Support for this research was provided by Peschl Ultraviolet GmbH and participated in the interpretation of data, review, and approval of this publication.

Acknowledgements

This work was supported through the German Ministry of Economic Affairs and Energy (BMWi), based on a resolution of the German Parliament within the AiF/ZIM project MISCOP, grant no. ZF4654701ZG8. The authors acknowledge support by the state of Baden-Württemberg through bwHPC and the German Research Foundation (DFG) through grant no. INST 40/575-1 FUGG (JUSTUS 2 cluster).

Notes and references

1 G. Ciamician, *Bull. Soc. Chim. Fr.*, 1908, **4**, 1–27.
2 P. T. Anastas and M. M. Kirchhoff, *Acc. Chem. Res.*, 2002, **35**, 686–694.
3 N. Hoffmann, *Photochem. Photobiol. Sci.*, 2012, **11**, 1613.
4 H. C. Erythropel, J. B. Zimmerman, T. M. de Winter, L. Petitjean, F. Melnikov, C. H. Lam, A. W. Lounsbury, K. E. Mellor, N. Z. Janković, Q. Tu, L. N. Pincus, M. M. Falinski, W. Shi, P. Coish, D. L. Plata and P. T. Anastas, *Green Chem.*, 2018, **20**, 1929–1961.
5 A. E. Cassano, C. A. Martin, R. J. Brandi and O. M. Alfano, *Ind. Eng. Chem. Res.*, 1995, **34**, 2155–2201.
6 K. Gilmore and P. H. Seeberger, *Chem. Rec.*, 2014, **14**, 410–418.
7 T. H. Rehm, *Chem. – Eur. J.*, 2020, **26**, 16952–16974.
8 M. Pasquali, F. Santarelli, J. F. Porter and P.-L. Yue, *AIChE J.*, 1996, **42**, 532–537.
9 A. E. Cassano and O. M. Alfano, *Catal. Today*, 2000, **58**, 167–197.
10 H. E. Bonfield, T. Knauber, F. Lévesque, E. G. Moschetta, F. Susanne and L. J. Edwards, *Nat. Commun.*, 2020, **11**, 804.
11 H. J. C. Jacobs and E. Havinga, in *Photochemistry of Vitamin D and its Isomers and of Simple Trienes*, John Wiley & Sons, Ltd, 1979, pp. 305–373.
12 M. Escribà-Gelonch, A. Halpin, T. Noël and V. Hessel, *ChemPhotoChem*, 2018, **2**, 922–930.
13 Y. Su, N. J. W. Straathof, V. Hessel and T. Noël, *Chem. – Eur. J.*, 2014, **20**, 10562–10589.
14 T. Aillet, K. Loubière, L. Prat and O. Dechy-Cabaret, *AIChE J.*, 2015, **61**, 1284–1299.
15 C. Rosso, S. Gisbertz, J. D. Williams, H. P. L. Gemoets, W. Debrouwer, B. Pieber and C. O. Kappe, *React. Chem. Eng.*, 2020, **5**, 597–604.
16 F. Gaulhofer, M. Metzger, A. Peschl and D. Ziegenbalg, *Ind. Eng. Chem. Res.*, 2023, **62**, 11456–11469.
17 M. E. Leblebici, G. D. Stefanidis and T. V. Gerven, *Chem. Eng. Process.: Process Intesif.*, 2015, **97**, 106–111.
18 K. Loubière, M. Oelgemöller, T. Aillet, O. Dechy-Cabaret and L. Prat, *Chem. Eng. Process.: Process Intesif.*, 2016, **104**, 120–132.
19 D. Cambié, C. Bottecchia, N. J. W. Straathof, V. Hessel and T. Noël, *Chem. Rev.*, 2016, **116**, 10276–10341.
20 V. Hessel, H. Löwe and F. Schönfeld, *Chem. Eng. Sci.*, 2005, **60**, 2479–2501.
21 S. Liu, A. N. Hrymak and P. E. Wood, *AIChE J.*, 2006, **52**, 150–157.
22 M. K. Singh, P. D. Anderson and H. E. H. Meijer, *Macromol. Rapid Commun.*, 2009, **30**, 362–376.
23 P. Hermann, J. Timmermann, M. Hoffmann, M. Schlüter, C. Hofmann, P. Löb and D. Ziegenbalg, *Chem. Eng. J.*, 2018, **334**, 1996–2003.
24 A. M. Díez, F. C. Moreira, B. A. Marinho, J. C. Espíndola, L. O. Paulista, M. Sanromán, M. Pazos, R. A. Boaventura and V. J. Vilar, *Chem. Eng. J.*, 2018, **343**, 597–606.
25 F. Guba, F. Gaulhofer and D. Ziegenbalg, *J. Flow Chem.*, 2021, **11**, 495–513.
26 D. S. Lee, M. Sharabi, R. Jefferson-Loveday, S. J. Pickering, M. Poliakoff and M. W. George, *Org. Process Res. Dev.*, 2020, **24**, 201–206.
27 C. Pratley, Y. Shaalan, L. Boulton, C. Jamieson, J. A. Murphy and L. J. Edwards, *Org. Process Res. Dev.*, 2023, DOI: **10.1021/acs.oprd.3c00348**.
28 I. Boiarkina, S. Norris and D. A. Patterson, *Chem. Eng. J.*, 2013, **225**, 752–765.
29 A. Chaudhuri, S. D. A. Zondag, J. H. A. Schuurmans, J. van der Schaaf and T. Noël, *Org. Process Res. Dev.*, 2022, **26**, 1279–1288.
30 H. Löwe, V. Hessel and A. Mueller, *Pure Appl. Chem.*, 2002, **74**, 2271–2276.
31 E. E. Coyle and M. Oelgemöller, *Photochem. Photobiol. Sci.*, 2008, **7**, 1313–1322.
32 T. Noël, in *Discovering the Future of Molecular Sciences*, Wiley-VCH Verlag GmbH & Co. KGaA, 2014, pp. 137–164.
33 W.-Y. Lin, Y. Wang, S. Wang and H.-R. Tseng, *Nano Today*, 2009, **4**, 470–481.
34 Z. He, Y. Li, Q. Zhang and H. Wang, *Appl. Catal., B*, 2010, **93**, 376–382.
35 M. Oelgemoeller, *Chem. Eng. Technol.*, 2012, **35**, 1144–1152.
36 L. D. Elliott, J. P. Knowles, P. J. Koovits, K. G. Maskill, M. J. Ralph, G. Lejeune, L. J. Edwards, R. I. Robinson, I. R. Clemens, B. Cox, D. D. Pascoe, G. Koch, M. Eberle, M. B. Berry and K. I. Booker-Milburn, *Chem. – Eur. J.*, 2014, **20**, 15226–15232.
37 T. Aillet, K. Loubière, O. Dechy-Cabaret and L. Prat, *Chem. Eng. Technol.*, 2016, **39**, 115–122.
38 R. Chen, X. Cheng, X. Zhu, Q. Liao, L. An, D. Ye, X. He and Z. Wang, *Chem. Eng. J.*, 2017, **316**, 911–918.
39 B. Wriedt, D. Kowalczyk and D. Ziegenbalg, *ChemPhotoChem*, 2018, **2**, 913–921.
40 A. Woitalka, S. Kuhn and K. Jensen, *Chem. Eng. Sci.*, 2014, **116**, 1–8.
41 Y. Su, K. Kuijpers, V. Hessel and T. Noël, *React. Chem. Eng.*, 2016, **1**, 73–81.
42 K. S. Elvira, R. C. R. Wootton, N. M. Reis, M. R. Mackley and A. J. deMello, *ACS Sustainable Chem. Eng.*, 2013, **1**, 209–213.
43 N. M. Reis and G. L. Puma, *Chem. Commun.*, 2015, **51**, 8414–8417.
44 D. Kowalczyk, P. Li, A. Abbas, J. Eichhorn, P. Buday, M. Heiland, A. Pannwitz, F. H. Schacher, W. Weigand, C. Streb and D. Ziegenbalg, *ChemPhotoChem*, 2022, **6**, e202200044.
45 D. Ziegenbalg, A. Pannwitz, S. Rau, B. Dietzek-Ivanšić and C. Streb, *Angew. Chem., Int. Ed.*, 2022, **61**, e202114106.
46 T. Noël and E. Zysman-Colman, *Chem Catal.*, 2022, **2**, 468–476.
47 K. Hölz, J. Lietard and M. M. Somoza, *ACS Sustainable Chem. Eng.*, 2016, **5**, 828–834.
48 L. Buglioni, F. Raymenants, A. Slattery, S. D. A. Zondag and T. Noël, *Chem. Rev.*, 2021, **122**, 2752–2906.
49 T. D. Svejstrup, A. Chatterjee, D. Schekin, T. Wagner, J. Zach, M. J. Johansson, G. Bergonzini and B. König, *ChemPhotoChem*, 2021, **5**, 808–814.

50 P. Piacentini, J. M. Fordham, E. Serrano, L. Hepp and M. Santagostino, *Org. Process Res. Dev.*, 2023, **27**, 798–810.
51 L. L. Simon, M. Dieckmann, A. Robinson, T. Vent-Schmidt, D. Marantelli, R. Kohlbrenner, A. Saint-Dizier, D. Gribkov and J.-P. Krieger, *Org. Process Res. Dev.*, 2021, **25**, 2221–2229.
52 T. V. Gerven and A. Stankiewicz, *Ind. Eng. Chem. Res.*, 2009, **48**, 2465–2474.
53 Ü. Taştan, J. Dollinger and D. Ziegenbalg, *Flow Meas. Instrum.*, 2018, **59**, 211–214.
54 D. Ziegenbalg, in *Selected Aspects of Photoreactor Engineering*, John Wiley & Sons, Ltd, 2021, ch. 7, pp. 155–186.
55 W. G. Vincenti and C. H. Kruger, *J. R. Aeronaut. Soc.*, 1966, **70**, 741–742.
56 S. E. Braslavsky, A. M. Braun, A. E. Cassano, A. V. Emeline, M. I. Litter, L. Palmisano, V. N. Parmon and N. Serpone, *Pure Appl. Chem.*, 2011, **83**, 931–1014.
57 J. Moreno, C. Casado and J. Marugán, *Chem. Eng. Sci.*, 2019, **205**, 151–164.
58 J. Moreno-SanSegundo, C. Casado, D. Concha, A. S. Montemayor and J. Marugán, *Open Research Europe*, 2021, vol. 1, p. 2.
59 S. Chandrasekhar, *Radiative Transfer*, Clarendon Press, 1950.
60 B. G. Carlson, *Transport Theory: Discrete Ordinates Quadrature Over the Unit Sphere*, Los Alamos National Lab. (LANL), Los Alamos, NM (United States), Technical Report, 1970.
61 K. D. Lathrop, *Nucl. Sci. Eng.*, 1966, **24**, 381–388.
62 W. A. Fiveland, *J. Heat Transfer*, 1984, **106**, 699–706.
63 C. Greenshields, *OpenFOAM v7 User Guide*, The OpenFOAM Foundation, London, UK, 2019.
64 M. Sender and D. Ziegenbalg, *Chem. Ing. Tech.*, 2017, **89**, 1159–1173.
65 A. K. Chibisov and H. Görner, *J. Phys. Chem. A*, 1997, **101**, 4305–4312.
66 H. Bouas-Laurent and H. Dürr, *Pure Appl. Chem.*, 2001, **73**, 639–665.
67 H. Görner, *Phys. Chem. Chem. Phys.*, 2001, **3**, 416–423.
68 M. Maafi and R. G. Brown, *Int. J. Chem. Kinet.*, 2007, **39**, 539–545.
69 A. S. Kholmanskii and K. M. Dyumaev, *Russ. Chem. Rev.*, 1987, **56**, 136.
70 C. J. Roxburgh, P. G. Sammes and A. Abdullah, *Dyes Pigm.*, 2011, **90**, 146–162.
71 H. Dürr and H. Bouas-Laurent, *Photochromism: Molecules and Systems*, Elsevier, 1990.
72 V. Malatesta, in *Photodegradation of Organic Photochromes*, Kluwer Academic Publishers, 2002, pp. 65–166.
73 H. A. Irazoqui, J. Cerdá and A. E. Cassano, *Chem. Eng. J.*, 1976, **11**, 27–37.
74 O. M. Alfano, R. L. Romero and A. E. Cassano, *Chem. Eng. Sci.*, 1986, **41**, 421–444.
75 G. E. Imoberdorf, F. Taghipour and M. Mohseni, *J. Photochem. Photobiol., A*, 2008, **198**, 169–178.
76 D. A. Sozzi and F. Taghipour, *Environ. Sci. Technol.*, 2006, **40**, 1609–1615.